AERODYNAMIC PREDICTIONS OF THE SHIP-HELICOPTER DYNAMIC INTERFACE WITH A DUAL-SOLVER HYBRID CFD METHODOLOGY

Alex M. Moushegian, amoushegian3@gatech.edu, Georgia Institute of Technology (USA)
Marilyn J. Smith, marilyn.smith@ae.gatech.edu, Georgia Institute of Technology (USA)

Abstract

Characterization of ship-helicopter dynamic interface (DI) aerodynamics is a challenging problem that must be addressed for safe naval helicopter operations. Current computational methods of simulating the DI employ highly expensive unsteady Reynolds-Averaged Navier-Stokes (uRANS) techniques that exceed the resources available for most applications. Newly-developed dual-solver hybrid computational fluid dynamics (CFD) techniques permit the resolution of the fundamental physics in the DI at up to 85% less computational costs compared to traditional methods through a reduction of the uRANS mesh size, faster initialization of the flow field, and decoupling of the ship and helicopter aerodynamic simulations. While detailed experimental data is not yet available, good qualitative agreement between fuselage loads in simulated DI scenarios with flight test vehicle accelerations is observed.

1. INTRODUCTION

Helicopter shipboard operations are characterized by a set of complex aerodynamic features that can result in difficult or dangerous scenarios for pilots. These conditions are termed the Dynamic Interface (DI) between the ship and helicopter. As the DI can vary significantly for different combinations of Naval assets and environmental conditions, testing of every combination of ship and helicopter at a variety of wind-over-deck (WOD) conditions is required to define safe operational guidelines. This testing is achieved through at-sea flight tests, which are expensive, difficult to schedule, and can present difficulty in replicating all WOD points depending on atmospheric conditions [1]. As a result, alternatives to this testing using computational models of the DI are sought to supplement and minimize the at-sea testing, as well at mitigate gaps that exist in the WOD operational envelopes.

The unsteady physics associated with even a simplified ship geometry, such as the Simple Frigate Shape 2 (SFS2), result in a highly complex three-dimensional unsteady flow, as depicted by the schematic developed from wind tunnel flow visualizations by Seth [2] in Fig. 1. The scarf vortices from ship superstructures create shear layers over the rotorcraft landing deck, which includes aerodynamic phenomena comparable to that of backward facing steps. As observed in Fig. 1, many of the upstream components are sharp edged, so that separation will be Reynolds number independent [3, 4]. Based on computational modeling, differences in the interactional vortex physics on the landing deck are present between subscale Reynolds numbers in the range of 100,000 to 400,000 and full scale Reynolds numbers that are two orders of magnitude higher. Prior publication of limited features note that vortex locations and recirculation bubbles are observed to have a 5% difference in location [3]. The impact of scaling should include large yaw angles with respect to the wind, as the complex shear layer and separated flow interactions can result in more significant differences than in a zero degree headwind (yaw is zero degrees) [5]. The influence of the wind tunnel walls can result in features that influence the ship interactions, including stronger shear layers and reattachment points on the ship landing deck [6]. As noted in Fig. 1, there are dynamically changing bistable features that can vary in character with the ship orientation. As air vehicles will be flying into this dynamically changing flow, it is important to ensure that computational approaches are able to predict not simply the mean flow, but the influence that these unsteady flowfields have on the terminal shipboard operations of rotary wing vehicles.

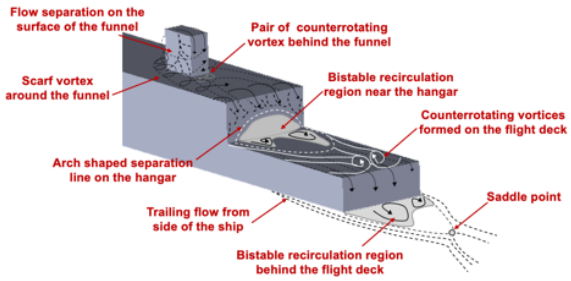

Figure 1: Schematic showing the development of the ship airwake flow structures interpreted from wind tunnel tests viewed from the ship stern. From Seth [2].

Research in computational techniques suitable for resolving the DI have defined two suitable approaches: "unified" and "coupled" methodologies. A unified approach employs a single monolithic solver to resolve the aerodynamics of both the ship and the helicopter simultaneously. To resolve the complex physics of the dynamic interface, it is often necessary to employ high-fidelity, unsteady Reynolds-Averaged Navier-Stokes (uRANS) solvers, typically with large eddy simulation (LES) turbulence closures in the large separated wakes. These approaches are expensive, requiring tens of thousands of computer hours, due to the large range of time and length scales involved in these interactional aerodynamics, requiring small computational time steps and highly refined computational grids to adequately resolve [7]. Employing momentum-theory-based models of the helicopter rotor can somewhat mitigate the time step and grid size restrictions of uRANS methods, but much of the expense is retained and the full physics of the rotor aerodynamics may not be captured [8, 9].

Coupled techniques separate the simulations of the ship and helicopter aerodynamics and make some attempt to merge the two models into a single representation of the dynamic interface. The most commonly applied method is to precompute the ship airwake and use the resulting airwake database as an input to a flight dynamics simulation of the helicopter. This one-way coupled approach can be employed in real-time and accounts for the broad nature of the ship airwake's effect on the helicopter aerodynamics, but detailed physical interactions between the rotor wake and the ship structure, ship airwake, and helicopter fuselage are not resolved [10]. Coupled approaches to DI modeling are not necessarily simple superpositions of flow fields. Depending on the formulation, the airwake will alter not only the flight characteristics encountered by the rotor/vehicle, but with a sophisticated rotor wake model and coupling procedure, the wake of the rotor is changed and this will provide a secondary influence on the interactional aeromechanics. This approach permits prediction of the first-order nonlinear aerodynamic coupling between the airwake and the rotor wake, as well as the use of the same airwake database for multiple test points or different helicopters.

The large gap in the cost/fidelity trade-off between unified uRANS and coupled flight dynamics simulations is not unique to DI analysis. The need for a middle-ground in rotorcraft computational fluid dynamics analysis has recently been addressed with the development of hybrid CFD methodologies which employ a dual-solver approach to aerodynamic modeling of the rotor wake. In the near-body close to the rotor blades, uRANS solvers are utilized to resolve the complex flow physics within the rotor disk. The far wake can be resolved with a variety of alternative aerodynamic solvers such as Vorticity Transport Methods (VTM) [11], Viscous Vortex Particle Methods (VVPM) [12], or Potential Wake Methods (PWM) [13, 14]. uRANS-PWM methods provide the most significant cost savings over full uRANS methodologies, with predictions of rotor hover performance and aeroelastic distributed loads within 10% of full uRANS at up to 95% reduced computational cost when employing a full-span free-vortex PWM [15, 16, 17, 18].

This research describes the development and application of OVERFLOW-CHARM, a hybrid uRANS-PWM solver, to the DI through replication of a Low-Speed Object-Induced Recirculation (LOIDR) flight test performed at Naval Air Warfare Command, Aircraft Division, Patuxent River (NAWCAD-PR).

2. COMPUTATIONAL METHODOLOGY

The hybrid dual-solver approach, OVERFLOW-CHARM, couples NASA's structured overset URANS solver OVERFLOW [19] and Continuum Dynamics, Incorporated's full-span free-vortex wake solver CHARM [20]. OVERFLOW's fourth- and sixth-order spatial differencing schemes accurately preserve vorticity and acoustic information on reduced-size meshes compared with solvers based on second-order schemes. Its oversetting capability allows resolution of complex geometries using multiple structured grids, so that it has been widely adopted within the both the fixed- and rotary-wing communities. OVERFLOW includes the native capability to compute rotor blade force and moment coefficients in various frames of reference, can track multiple rotors with arbitrary properties and can be coupled with comprehensive rotorcraft analysis tools like RCAS [21] and ANOPP2 [22] for aeroelastic and aeroacoustic predictions, respectively. These

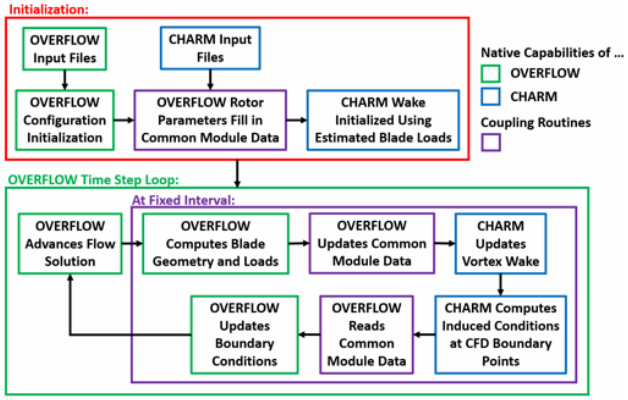

Figure 2: Flowchart describing the operation of OVERFLOW-CHARM

features have resulted in OVERFLOW's inclusion as an integrated component of many existing rotorcraft analysis workflows, such as HPCMP CREATE™-AV Helios [23].

CHARM represents rotor wakes as a series of constant strength vortex filaments released along the span of the rotor blades according to the blade circulation distribution. The vortex filaments are discretized using curved vortex elements that provide superior computational efficiency over linear segments and improve the scalability of the solver [20]. Aerodynamic bodies such as hubs, fuselages, wings, and ground obstacles can be resolved with doublet panels within CHARM or modeled via alternate methods, such as OVERFLOW. CHARM has also been successfully and accurately applied to numerous rotorcraft and advanced air mobility (AAM) vehicle analyses [24, 25, 26, 27].

The coupling framework of OVERFLOW-CHARM is described in Fig. 2. The OVERFLOW and CHARM solutions communicate through the OVERFLOW-computed blade loads and the CHARM-computed wake domain boundary flow conditions. This approach permits the uRANS computational domain to be significantly reduced compared to a conventional uRANS simulation while still including the effects of the full rotor wake. Components of interest can be modeled either with uRANS (OVERFLOW) through Navier-Stokes domains or potentially (CHARM) using image planes or doublet panels. In this way, obstacles, such as buildings, ship decks, and the ground planes can be included in analysis of full or partial blockage or ground effect [18].

This framework has been proven to accurately resolve rotor loads (airloads, structural loads, hub loads) with the same level of fidelity (within 5%) of conventional uRANS methods at reduced computational costs of approximately 60-90%, depending on the flight condition [15, 16]. Multiple improvements to the accuracy, efficiency, and flexibility of the coupling framework have since been implemented and validated for relevant rotorcraft configurations for rotor-wing interactions and ground effect [18, 28].

To investigate OVERFLOW-CHARM's ability to resolve the dynamic interface configurations of interest, the mechanics to couple the code to an externally-computed airwake database were implemented. This coupling approach provides the influence of the ship airwake on the rotorcraft. While previous coupled methods have shown discrepancies as the vehicle approaches the shipboard [10], this is attributed to the lack of modeling of the aerodynamic interactions between the ship and rotor wake, which is included in the current approach. As the airwake database only needs to be generated once for each wind-over-deck (WOD) condition, this approach is highly cost-effective to assess different rotor flight conditions for each WOD. The external airwake database, which is the ship configuration without the rotor model present, can be computed using time steps 10-50 times larger than that required for resolved rotor blades as the time step requirement is driven by large-scale, low-speed convecting eddies rather than by high-speed rotor blade motion. The larger time step translates directly to computational cost savings. The database is formed through a uniform Cartesian sampling of the resulting airwake at relevant spatial and temporal scales to encapsulate the expected range of aircraft operations.

The database is integrated into the OVERFLOW-CHARM simulation at each time when the CHARM wake is updated. CHARM calls the custom ship airwake coupling routine, which loops over the CHARM wake control points and uRANS boundary points, interpolates the velocities from the airwake database onto the point, and adds the resulting velocity to the existing velocity at the point. As long as the airwake database is a uniformly spaced Cartesian grid, the cell wherein the CHARM point lies can be calculated directly. Thus, the cost of the coupling scales directly and only with the number of points in the CHARM simulation, and the airwake database can be arbitrarily large (within memory constraints) without impacting the speed of the algorithm. As noted previously, this approach is not simply a superposition of flow fields, because the EFP airwake alters the CHARM rotor wake solution, which impacts the self-induced wake-element Biot-Savart calculations that are fed to OVERFLOW when the CHARM solution is advanced. Thus the nonlinear effects of the complex flow field are captured, though the resulting influence of the helicopter on the airwake is not included.

Table 1: Table of wind speed and orientation for the LOIDR tests.

	Downwind	**Sideslip**
β (°)	0	75
$\boldsymbol{M}_\infty$	0.0075	0.0083

3. FLIGHT TEST CAMPAIGN

Flight tests of the V-22, UH-72, OH-58C, and UH-60L have been performed on the airfield at Naval Air Warfare Command, Aircraft Division at Patuxent River, Maryland (NAWCAD-PR) with the objective of providing validation data for the Dynamic Interface Virtual Environment (DIVE) program to improve and validate DI simulation tools. The ground obstacle, called the Elevated Fixed Platform (EFP), was a 96×100×38 foot construction of standard CONEX boxes. During these tests, velocity data was obtained from anemometers arranged along the wall of the EFP, as well as aircraft performance data and ambient wind conditions from a reference anemometer. Rotor speed was varied to achieve different values of thrust coefficient, since aircraft weight was allowed to vary with fuel burned. The data gathered during the flight test includes time-resolved velocity measurements near the EFP, aircraft position and attitude, pilot and stability augmentation system (SAS) control inputs, and engine power and fuel consumption. Testing was performed on days where winds were not expected to exceed ten knots. Before each test, a hover ladder, during which the aircraft hovered at skid heights above the ground of 1, 6, 15, 24, 39, and 44 feet, was performed at a distance outside of the influence of the EFP. Next, the hover ladders were repeated for predetermined locations approaching the EFP along a line extending from the centerline of the EFP. Finally, a similar procedure was performed with the rotor aligned with the port face of the EFP. A snapshot of the UH-60L during these tests, which are described in detail in Silva et al. [29], is given in Fig. 3. Because the data are still undergoing analysis prior to being released, to facilitate this demonstration, the unprocessed accelerometer data were qualitatively compared to computational predictions as described in subsequent sections.

Figure 3: UH-60L hovering near the EFP during flight tests at NAWCAD-PR. Photo courtesy of NAVAIR [29].

4. NUMERICAL APPROACH

From the full-scale LOIDR flight test campaign, test points for the hovering UH-60L at a skid-height of fifteen feet (corresponding to approximately one rotor radius), 98% rotor speed, and two different locations with respect to the EFP have been computationally analyzed. At the first location, the UH-60L hovers 34 feet from the nearest face of the EFP, measured to the pilot's "bumline". For the second location, the UH-60L hovers over open tarmac, providing a comparison of the aerodynamics when the rotor wake is (Loc A) and is not (Loc B) interacting with the EFP. The wind conditions during these tests were approximately 5.5 knots at 217° from north, corresponding to 75 degree sideslip. To examine the influence of the wind direction, a second case with winds directly aligned with the EFP center line (zero degree helicopter sideslip) at five knots were also performed at Loc A. Table 1 defines these wind test conditions. Simulations were performed at standard sea level conditions with a rotor tip Mach number of 0.63.

The airwake database was generated using HPCMP CREATE™-AV Kestrel [30]. From these simulations, airwake data were extracted for a 300×300×150 foot control volume around the helicopter position of the EFP at the recorded ambient wind conditions. The airwake database was coupled to an OVERFLOW-CHARM simulation of the UH-60L helicopter at identical reference conditions. This process is illustrated in Fig. 5.

4.1. Airwake Database

The airwake database was formed via three stages. First, a steady simulation developed the EFP wake. Then, a time-accurate simulation prior to data extraction evolved accurate unsteadiness in the wake. Finally, a second time-accurate simulation generated the final airwake data, extracted onto the three-dimensional Cartesian grid described previously. The extracted data were converted to a simplified format containing only velocity deviations from the nominal freestream velocity and normalized by the freestream

speed:

$$\vec{u}_{airwake} = \frac{\vec{u}_{extract} - \vec{u}_{\infty}}{\|\vec{u}_{\infty}\|}. \quad (1)$$

This circumvents the need for unit conversions between the airwake and helicopter simulations.

The computational mesh for the airwake simulations was an unstructured mesh composed of tetrahedral, prism, and pyramid cells generated by the program Heldenmesh [31, 32, 33] (see Fig. 4). Heldenmesh merges a list of patches and an input file describing sources for grid refinement to create the unstructured surface and volume meshes. The EFP has a primary cell spacing one-foot, with half-foot cells along the edges. A refinement region was introduced in the operational area of the helicopter containing one-foot cells. The cell sizes gradually grow from the refinement region with an initial stretching factor of 1.05 to a maximum size of fifty feet. The far field boundaries are approximately 5000 feet from the EFP and the top of the bounding box is 1000 feet high. Boundary layer T-Rex cells are grown from the ground plane and EFP surfaces with a first cell spacing of 0.0000132 feet, which corresponds to a $y^+ \leq 1$. The grid contained a total of 81 million cells.

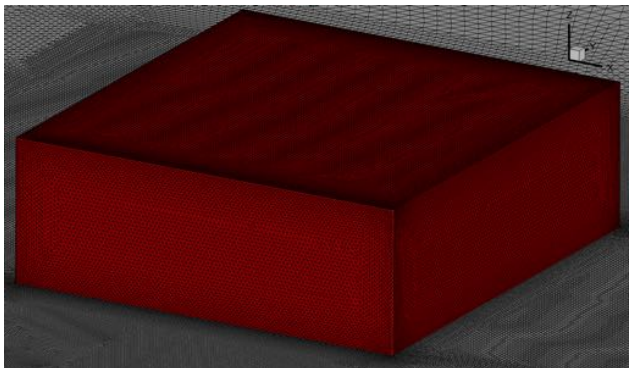

(a) EFP Surface Grid

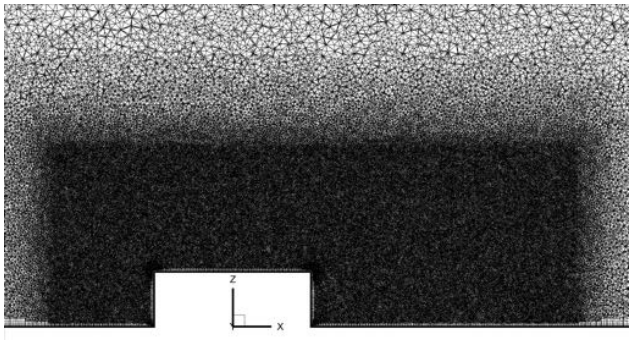

(b) Volume Mesh Slice

Figure 4: Illustrations of the unstructured EFP grid employed in the Kestrel airwake simulations.

The computations for the airwake development employed the compressible formulation of the default near-body solver in Kestrel, KCFD [8]. The flow was resolved with an HLLE++ scheme for inviscid flux computation, LDD+ scheme for viscous flux computation, second-order spatial accuracy, and the Menter SST DDES turbulence model with a wall function. The steady state simulations were evaluated for 30000 iterations at a Courant-Freidrichs-Lewy (CFL) number of 1000 to develop the airwake. The unsteady simulations employed second-order Newton time stepping with a time step corresponding to 1000 steps for a fluid particle to traverse the length of the EFP at the freestream velocity (about 0.01 seconds per step). Four subiterations were utilized, which was sufficient to provide a residual drop of at least three orders of magnitude. The unsteady flow field was initialized for 20000 iterations, and then another 2160 iterations were performed to generate the airwake extracts. This procedure and mesh development follows best practices recommended by Dr. Susan Polsky, established from decades of ship airwake simulation experience at NAWCAD-PR.

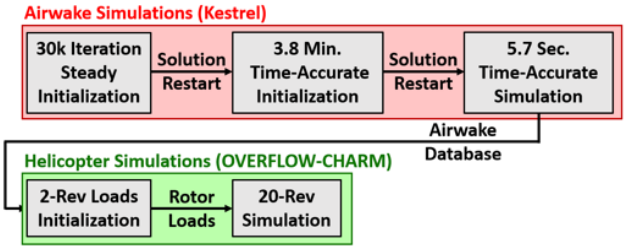

Figure 5: Flowchart of procedure for performing LOIDR simulations.

The airwake simulations were required to produce a time history of airwake data that exceeded the length of time over which OVERFLOW-CHARM predicted the rotorcraft response. To allow sufficient time for the simulation to converge and investigate unsteady fuselage and rotor loads, an airwake record length of 20 rotor revolutions was chosen. At the experimental rotor speed, this corresponds to 4.7 seconds of simulation, with an extra second required to initialize the CHARM wake. The extract volume, shown in Fig. 6, encompasses the region of space in which the CHARM wake is modeled in the helicopter simulations and is made up of Cartesian cells at a resolution of one-foot (0.6 blade chords).

5. Helicopter Simulations

The details in obtaining the UH-60L simulations employed lessons learned from the previous studies of the relevant aerodynamics in DI analysis by NAVAIR. The rotor blades were resolved with non-contiguous

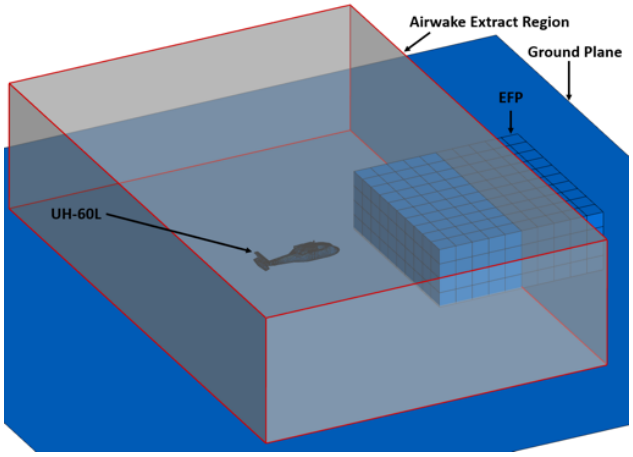

Figure 6: Airwake database region with respect to the EFP and UH-60L

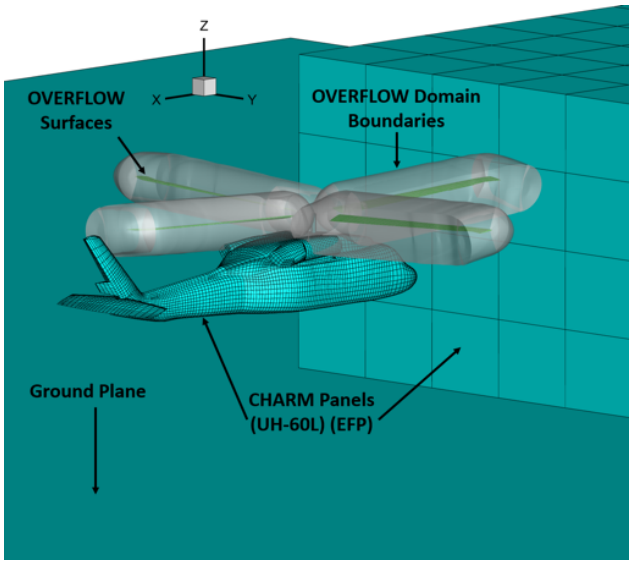

Figure 7: Diagram of the OVERFLOW-CHARM domain configuration.

OVERFLOW grids (see Fig. 7). The fuselage and EFP were resolved with CHARM doublet panels. The ground was modeled as an image plane. Because transformations of the pilot controls to swashplate angles were not provided, cyclic angles were held at zero and the collective was trimmed by first computing a target rotor thrust based on gross weight and fuselage download. The fuselage download was calculated directly from pressures computed by the OVERFLOW-CHARM fuselage panel method. The gross weight was calculated from flight test data, where the empty weight of the helicopter and pilot weights were given. Fuel weight was calculated by subtracting the total fuel burned from the reported starting fuel. The total fuel burned was calculated by integrated the measured fuel burn rate from the start of the data collection period to the appropriate time of the selected test point, accounting for incremental burn during the simulated period. A blade motion file with the updated collective to either increase or decrease the predicted thrust to approach the target thrust was generated. The rotor coning angle was approximated from previous aeroelastic predictions of the UH-60 rotor assuming linearity with thrust. No elastic deflections of the blades were applied. This manual trimming procedure is in lieu of coupling to a flight dynamics or comprehensive code that is recommended for future expansion of this analysis.

5.1. Computational Meshes

The OVERFLOW blade grids were identical to the baseline blade grids employed in the study of Wilbur et al. [34, 16], which studied the ability of OVERFLOW-CHARM to make aeroelastic predictions of the UH-60 rotor. The grids were originally generated at Boeing and are typical for engineering applications, and were part of a much larger mesh refinement study. Each near-body blade grid consists of three million points and is composed of a main blade C-mesh bounded by root and tip cap meshes. The surface of the blade is resolved by 302 points around the chord and 100 radial points, with 77 points extending in the wall-normal direction. The leading and trailing edge spacing corresponded to 0.3% and 0.05% of the reference chord, respectively. The first cell in the boundary layer had a thickness such that $y^+ = 1$, and there were approximately 46 points in the boundary layer.

The EFP and UH-60L fuselage were resolved with CHARM doublet panels. The UH-60L fuselage was represented with 8,374 triangular and quadrilateral panels, as illustrated in Fig. 8. This resolution was determined to be sufficient to resolve the geometry of the UH-60L and is much more detailed than is usually employed for stand-alone CHARM computations [35]. The EFP was made up of 220 rectangular panels, with ten panels along the length and width and four panels in the vertical direction.

5.2. Numerical Options

The selection of the optimum numerical options was derived from best practices established in previous studies with OVERFLOW-CHARM [28]. The physical time step is equivalent to a rotor advancement of 0.5 degrees, applying dual time steps with forty subiterations and a minimum CFL number of five, which provided a residual drop of at least one order of magnitude. The right-hand-side terms were discretized using fourth-order Roe upwind spatial differencing with 4/2 dissipation where the fourth- and second-order dissipation constants were 0.04 and 10.0, respectively. The left-hand-side terms were discretized using a diagonalized Beam-Warming scalar pentadiagonal scheme with

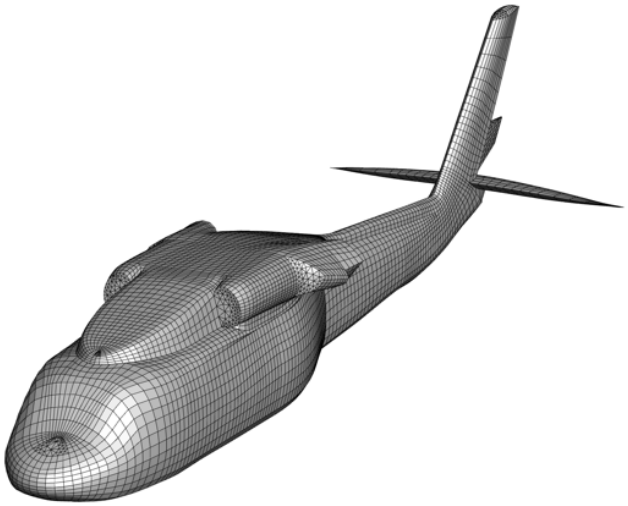

Figure 8: CHARM panels resolving the UH-60L fuselage.

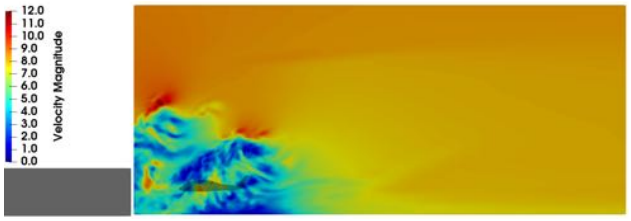

(a) Steady Restart

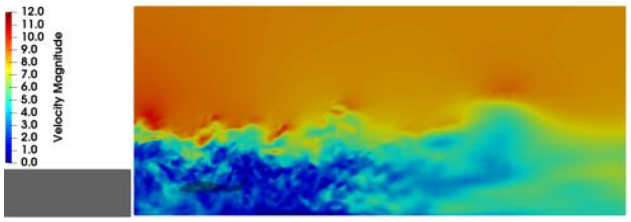

(b) Unsteady Restart

Figure 9: Slice of solution after steady-state and unsteady initialization calculations for the downwind airwake (fuselage not present in the simulation). EFP shown in gray.

fourth-order dissipation. The one-equation thin-layer SA turbulence model was applied with a rotational correction, as the flow over the rotor blades remains attached.

The CHARM model consisted of the EFP and UH-60L panels described earlier along with an image plane at ground level to resolve wake-body interactions. The CHARM rotor wake model was updated every five degrees of rotor rotation, retaining ten revolutions of full-span vortex elements and 20 revolutions of tip vortex elements. Artificial dissipation was applied near the ground plane to model the viscous interactions of the wake with the ground, as recommended by CDI. The CHARM solution was initialized for six revolutions from blade loads predicted by a two-revolution OVERFLOW simulation. To prevent initial uRANS transients from disrupting the CHARM solution, blade loads were blended from the input loads beginning after one blade passage of coupled simulation and proceeding over the second blade passage, after which loads are extracted solely from the uRANS solution.

6. RESULTS

6.1. EFP Airwake Predictions

The airwake simulations were performed on the US Department of Defense (DoD) high performance computing cluster "Onyx" using 704 Intel E5-2699v4 Broadwell processors at 2.8 GHz. Each calculation required approximately sixty hours of wall time, translating to about 42,000 CPU-hours. 92% of this time was spent initializing the flow field before airwake database extraction. Because the airwake extraction portion of the simulation constitutes such a small fraction of the total airwake development, lengthening the record length of the airwake database would not incur significant additional cost in the airwake simulations for applications where long record lengths of airwake data are required, i.e. a fully simulated shipboard approach.

Examples of the flow field planes after each stage of flow field initialization are illustrated in Figs. 9 and 10. Because mesh refinement only extends 172 feet in the x-direction behind the EFP, the steady-state simulation of the downwind case is unable to develop the airwake beyond this distance. The unsteady initialization further develops the airwake and time-accurately resolve the unsteadiness in the separated flow. At the sideslip condition, the unsteady initialization also resolves the secondary wake that is shed from the lower corner of the EFP, observed directly below the UH-60L position in Fig. 10.

The complexity of fully-developed airwakes for the downwind and sideslip conditions are illustrated in Fig. 11, with the location of the UH-60L in the coupled simulations displayed for reference. At the downwind condition, the UH-60L is fully immersed in the airwake of the EFP, whereas in the sideslip condition, the shear layer at the boundary of the airwake impinges directly on the UH-60L fuselage. As observed in Fig. 12, which illustrates a time-history of the cardinal velocities along the center line of the eventual UH-60L fuselage position, full immersion within the airwake results in velocity fluctuations of approximately six ft/s. In Fig. 13, velocities are much more variable in both space and time, with fluctuations as much as ten ft/s. The dominant period for oscillations is approximately

(a) Steady Restart

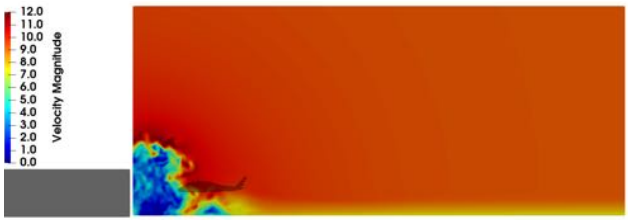

(b) Unsteady Restart

Figure 10: Slice of solution after steady-state and unsteady initialization calculations for the sideslip airwake (fuselage not present in the simulation). EFP shown in gray.

1-2 seconds in time and 5-10% of the fuselage length in space. The magnitude and temporal and spacial frequencies of these oscillations indicate that strong forces and moments are expected to be imparted on the fuselage in the coupled simulation at the sideslip condition, particularly side force and yawing moment from the airwake impinging on the nose of the fuselage.

6.2. OVERFLOW-CHARM Downwind Condition Simulations

6.2.1. Flow Field

Observing the CHARM-induced flow fields after 1.6 seconds of simulated time at the downwind condition condition in Fig. 14, the effect of airwake coupling is most clearly visible by its effect on the trajectory of the rotor wake. Without airwake coupling, the CHARM vortex wake elements are convected by the full freestream velocity, and the rotor wake behaves as if it were in traditional forward flight, with some impingement of the blade tip vortices on the nose of the fuselage. With airwake coupling, the CHARM vortex wake elements are instead immersed in the wake of the EFP and are convected by the low-speed flow in this separated region. As a result, the wake behaves more like a hover condition, and wake spreading due to the ground effect causes the blade tip vortices to pass well in front of the fuselage nose. The change in wake trajectory also determines how the blade tip vortices interact with the stabilator. Some recirculation of the rotor wake is observed in the high velocity region near the EFP face, but blade tip vortices are generally dissipated by the time they rise to the rotor

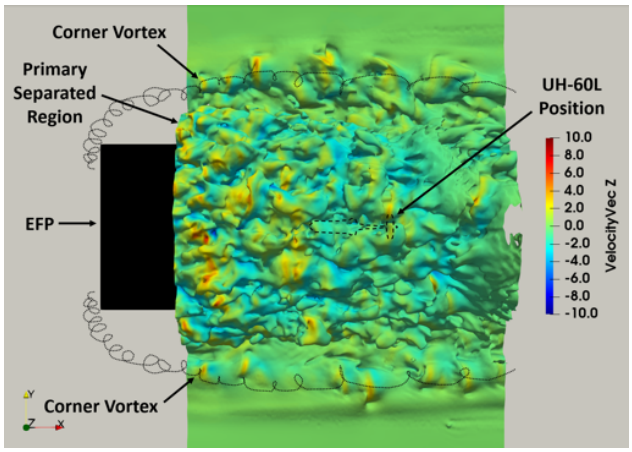

(a) Downwind Condition

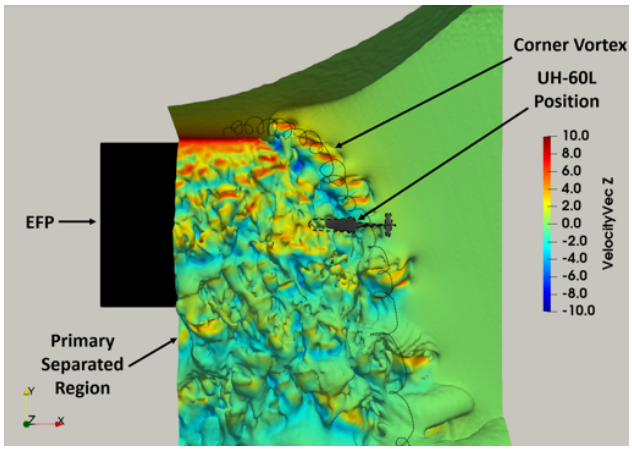

(b) Sideslip Condition

Figure 11: Isosurfaces of velocity magnitude colored by upwash velocity at the midpoint of the airwake database record (fuselage not present in the simulation). EFP shown in black.

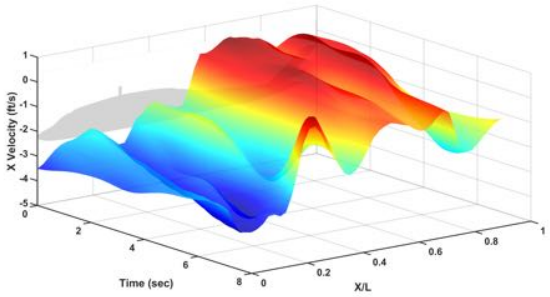

(a) Longitudinal Velocity

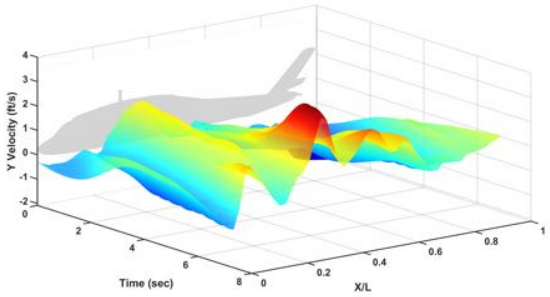

(b) Side Velocity

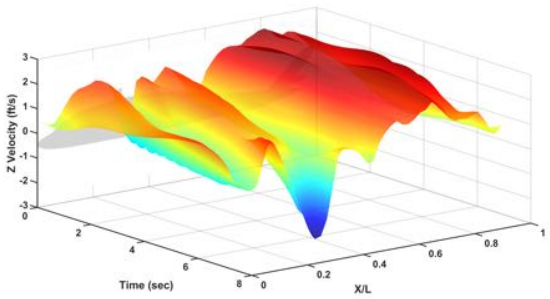

(c) Vertical Velocity

Figure 12: Time history of airwake velocities at the UH-60L hover location for the downwind airwake (fuselage not present in the simulation).

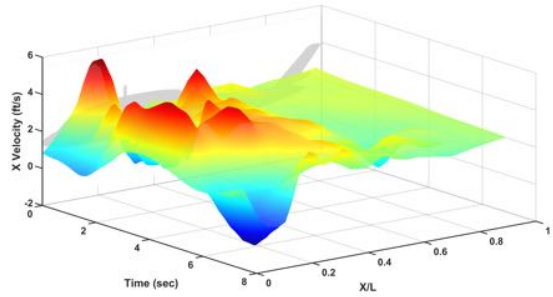

(a) Longitudinal Velocity

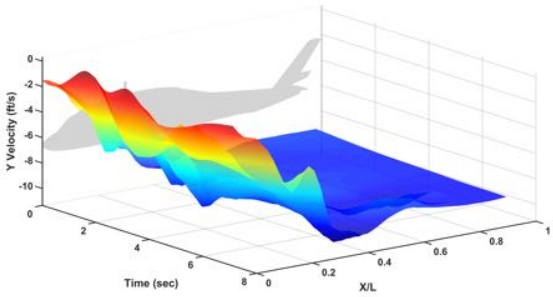

(b) Side Velocity

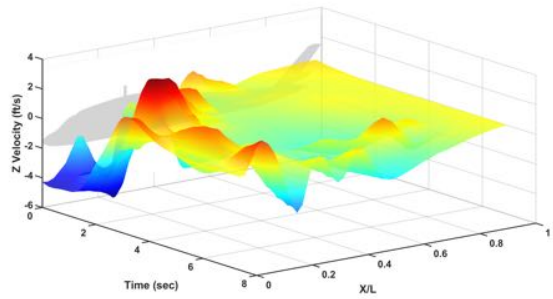

(c) Vertical Velocity

Figure 13: Time history of airwake velocities at the UH-60L hover location for the sideslip airwake (fuselage not present in the simulation).

plane.

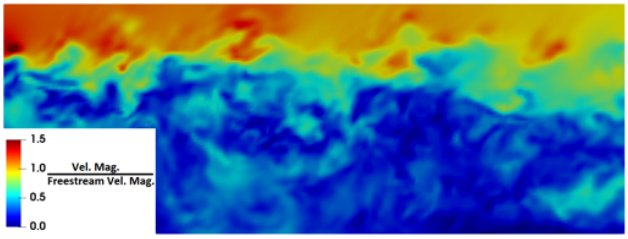

(a) EFP Airwake

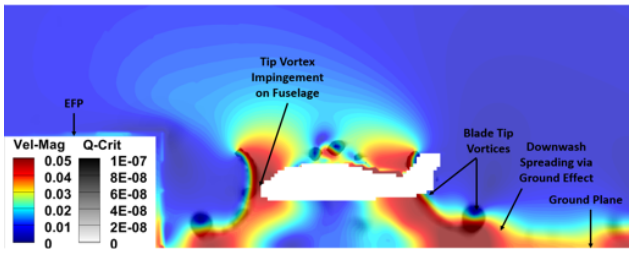

(b) No Airwake Coupling

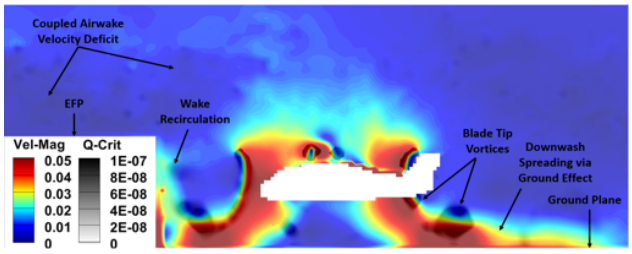

(c) With Airwake Coupling

Figure 14: Comparison of CHARM-induced flow fields at t = 1.6 seconds for OVERFLOW-CHARM simulations of the downwind condition with and without airwake coupling.

6.2.2. Fuselage Loads

While a major metric of interest during DI operations is pilot workload, it is generally quantified with subjective pilot assessments during flight tests that are not part of this work. When attempting to correlate wind tunnel or computational aerodynamic predictions to pilot workload, previous authors have determined that the most important factor is unsteadiness in the helicopter fuselage loads, particularly side and drag forces [36]. Making quantitative correlations of predictions of fuselage loads by OVERFLOW-CHARM to vehicle motion, pilot control inputs, and workload is left for future work, but qualitative comparison is made to investigate the capabilities of airwake-coupled OVERFLOW-CHARM simulations. The fuselage loads were filtered using a moving average filter:

$$F_{filtered}(t) = \overline{F_{raw}\,(t - t_b/2 : t + t_b/2)}. \quad (2)$$

where t_b is the temporal length of one blade passage. This equation filters out oscillations at and above the blade passage frequency, which dominate the time histories of the fuselage loads. Because the blade passage frequency (16.9 Hz) is high enough that the resulting oscillations do not require a pilot response to counteract and are instead perceived as vibrations and structural noise, the filtered loads provide a better indication of variations in forces and moments that will affect aircraft motion. The reference point for reported moments is the origin of the computational domain, located at the center of the rotor disk.

The impact of including airwake coupling in the OVERFLOW-CHARM simulations was investigated by comparing fuselage loads predicted with and without airwake coupling at the downwind condition. The most prominent influence on the statistics (see Table 2) is a drop in the mean longitudinal force, resulting from the immersion of the fuselage within the separated flow region of the EFP. The Root-Mean-Squared (RMS) forces and moments are also reduced by about 39% with the inclusion of airwake coupling, likely due to the reduced velocity magnitudes within the EFP airwake and the difference in the rotor wake trajectory. The reduction in fuselage force variation indicates that airwake coupling is necessary for accurate characterization of aircraft motion when the helicopter is operating in large regions of separated flow.

6.3. OVERFLOW-CHARM Sideslip Condition Simulations

6.3.1. Flow Field

Figure 15 compares the OVERFLOW-CHARM-predicted flow fields after 2.8 seconds of simulated time at the sideslip condition for three different instances: without the EFP, with the EFP and no airwake coupling, and with the EFP including airwake coupling. Without the EFP, the flow field corresponds to that of a helicopter in ground effect, for which this OVERFLOW-CHARM approach has been validated with OVERFLOW alone and with experiment [28, 18]. Behind the fuselage, interactions of the blade tip vortices and the UH-60L tail result in more dispersed vortices than at the nose. When the EFP panels are included in the model, rotor wake upwash is observed at the face of the EFP and tip vortices recirculate towards the rotor plane. Tip vortices at the front of the aircraft coalesce into larger vortices, whereas without the EFP, they remain spread along the slipstream boundary. When airwake coupling is included, these tip vortices again become spread along the slipstream boundary, and more pronounced rotor wake recirculation is observed. The velocity deficit within the separated flow region of the EFP airwake is clearly visible in the region around the EFP. The fully coupled flow fields at both the sideslip and downstream conditions contain the major features of the DI including sepa-

Table 2: Table of OVERFLOW-CHARM-predicted fuselage force and moment statistics at the sideslip condition. Forces are in lbs, moments are in lb-ft.

Simulation Configuration	**Long. Force**		**Side Force**		**Vertical Force**	
	Mean	**RMS**	**Mean**	**RMS**	**Mean**	**RMS**
No Airwake	181	100	-39	159	48	111
With Airwake	53	44	45	72	21	84
Simulation Configuration	**Roll Moment**		**Pitch Moment**		**Yaw Moment**	
	Mean	**RMS**	**Mean**	**RMS**	**Mean**	**RMS**
No Airwake	-66	983	1305	790	-66	983
With Airwake	474	469	1345	700	-262	607

rated flow from bluff body structures, deflection of the rotor wake with solid surfaces, rotor wake recirculation at solid walls, and rotor wake interactions with the helicopter fuselage. To improve the consistency of achieving these promising results, methods for enhancing the prediction of corner flows in the CHARM panel method should be investigated. Artifacts in the induced flow field in the form of high velocities at a single point very near the fuselage and EFP (see Fig. 15d), are the result of the panel method enforcing no slip across the panels. Because this is an induced flow field and not directly representative of the CHARM solution, these artifacts do not impact the fidelity of the CHARM solution.

6.3.2. Fuselage Loads

At the sideslip condition, the differences in predicted fuselage loads between simulations with and without the EFP and with and without airwake coupling are less pronounced than the downwind condition. No clear trend is visible for the influence of the EFP on the fuselage force statistics in Table 3, although the instantaneous forces are heavily influenced by the presence of the EFP. When airwake coupling is included, the mean longitudinal force drops from about 75 lbs to 31 lbs. As with the downwind condition, RMS forces and moments are generally reduced when airwake coupling is included, though only by 17% at this condition. Instantaneous fuselage loads are provided in Ref. [28].

6.4. Correlating Fuselage Loads to Flight Test Acceleration Measurements

The flight test data provides time histories of aircraft acceleration at the sideslip condition with and without the EFP. As a preliminary step towards correlating the fuselage forces to aircraft motion, "events" in the fuselage forces and flight test accelerations are compared. Events are classified by their temporal length, and are are defined as deviations of that length from the trend in the signal. Full details of event identification are provided in Ref. [28].

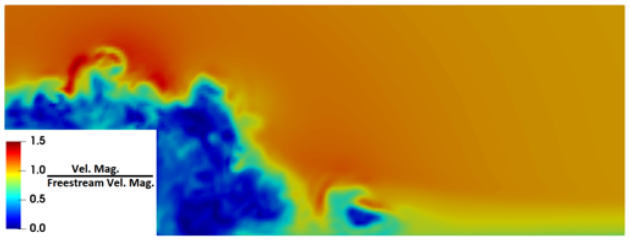

(a) EFP Airwake

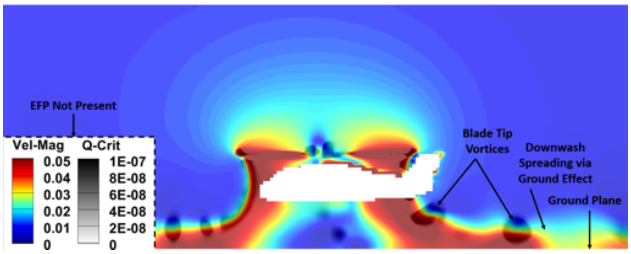

(b) No EFP

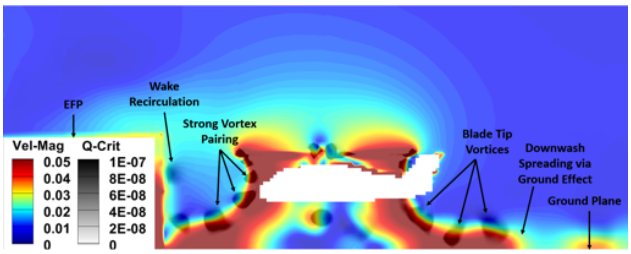

(c) With EFP (No Airwake Coupling)

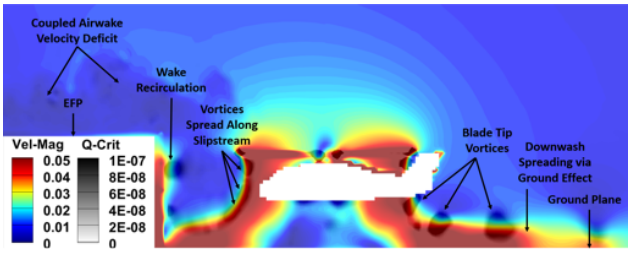

(d) With EFP (With Airwake Coupling)

Figure 15: Comparison of CHARM-induced flow fields at $t = 2.8$ seconds for OVERFLOW-CHARM simulations of the sideslip condition with and without the EFP present and with and without airwake coupling.

Table 3: Table of OVERFLOW-CHARM-predicted fuselage force and moment statistics at the sideslip condition. Forces are in lbs, moments are in lb-ft.

Simulation Configuration	**Long. Force**		**Side Force**		**Vertical Force**	
	Mean	**Variance**	**Mean**	**Variance**	**Mean**	**Variance**
No EFP	76	148	-192	179	71	102
EFP, No Airwake	74	150	-124	212	73	84
EFP, With Airwake	31	89	-197	161	69	90
Simulation Configuration	**Roll Moment**		**Pitch Moment**		**Yaw Moment**	
	Mean	**Variance**	**Mean**	**Variance**	**Mean**	**Variance**
No EFP	-1195	1072	893	1835	37	604
EFP, No Airwake	-775	1313	776	1882	-61	639
EFP, With Airwake	-1262	962	1090	1502	-84	354

Events are categorized by their length in seconds and the frequency of events having various lengths are compared between the fuselage longitudinal and side forces and flight test longitudinal and lateral accelerations, illustrated in Fig. 16. The most common events in both the flight test and computational data have lengths between 0.2 and 0.8 seconds, generally decreasing in frequency as event length increases. While OVERFLOW-CHARM generally overpredicts the frequency of events, likely due to somewhat exaggerated unsteadiness in the CHARM vortex wake method, which is a known aspect of potential wake models, the qualitative trend is captured. Events longer than one second occur infrequently in all data sets, and due to the relatively short record length of the OVERFLOW-CHARM data (4.7 seconds compared to 50 seconds for the flight test), these longer events are more difficult to correlate to the flight test controls data. The most prominent effect of the EFP in the flight test data is the increase in occurrence rate of events between 0.2 and 0.4 seconds, which is also predicted by OVERFLOW-CHARM. The occurrence rate of longer events in both the flight test data and OVERFLOW-CHARM predictions are less affected by the presence of the EFP and its airwake. These qualitative assessments with the accelerometer data indicate the efficacy of this approach.

6.5. Computational Cost

Conventional uRANS simulations of configurations such as this one have the primary disadvantage that the rotor and ship (in this case, replaced with the EFP) airwakes must be developed using the same time step. While the ship airwake can be initialized at a larger time step before the helicopter is placed into the simulation, once the rotor blades are turning, the entire fluid domain must be computed at the time step constrained by the motion of the rotor blades. For such simulations to be tractable, the rotor-constrained time step is typically avoided by using actuator disk methods, which sacrifice the time-accurate capture of rotor wake physics. With this OVERFLOW-CHARM methodology, the "ship" airwake is initialized ahead of time, but during the time period of interest, the ship airwake solver is constrained to the time step of the free-wake solution (e.g. five degrees of rotor rotation), rather than the uRANS time step of the rotor (e.g. 0.5 degrees of rotor rotation).

An additional source of computational cost in uRANS simulations is performing domain connectivity of the overlapping grids as the helicopter moves relative to the ship and as the blades move relative to the helicopter. Polsky et al. [10] reported that this procedure alone accounted for 54% of the CPU time per step of uRANS DI analysis when the helicopter is close to the ship. With the non-contiguous OVERFLOW-CHARM methodology utilized in this research, domain connectivity is only performed between the grids for each blade and amounts to less than 1% of the CPU time per step.

In total, the analyses presented here required 2,800 CPU-hours per second of simulated time for each test point. If the monolithic approach using only uRANS (rather than the hybrid code) is applied to the UH-60L, employing the same blade grids (12.3 million points) and an additional 20 million point uRANS fuselage grid, the computational cost would be approximately 19,000 CPU-hours per second of simulated time, including the additional cost of performing domain connectivity. As such, OVERFLOW-CHARM constitutes an estimated 85% cost savings compared to an equivalent uRANS simulation of the same configuration. The analyses of Polsky et al. [10] required 5,000 CPU-hours per second of simulated time for an actuator disk rotor model and a relatively coarse mesh of only 17 million total points for the ship and helicopter.

The addition of airwake coupling to the OVERFLOW-CHARM interface protocols increased the CHARM step time from 26.26 seconds to 27.18 seconds, demonstrating that the interface

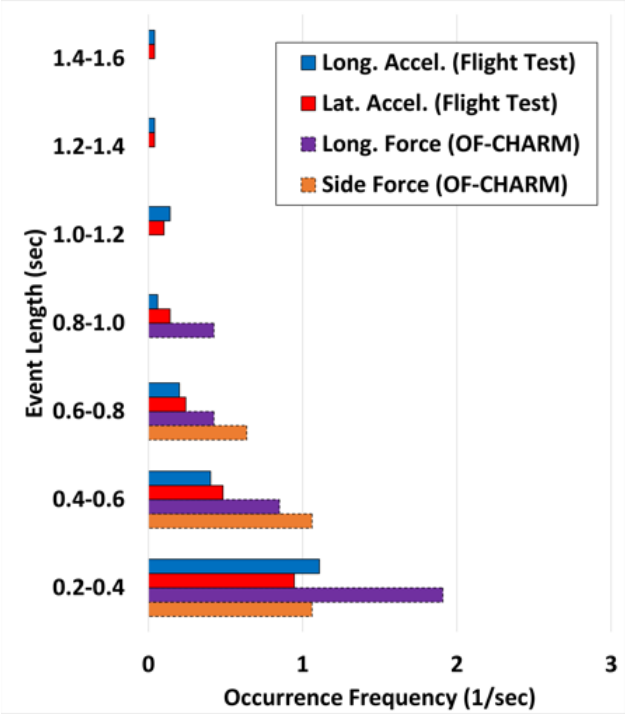

(a) No EFP

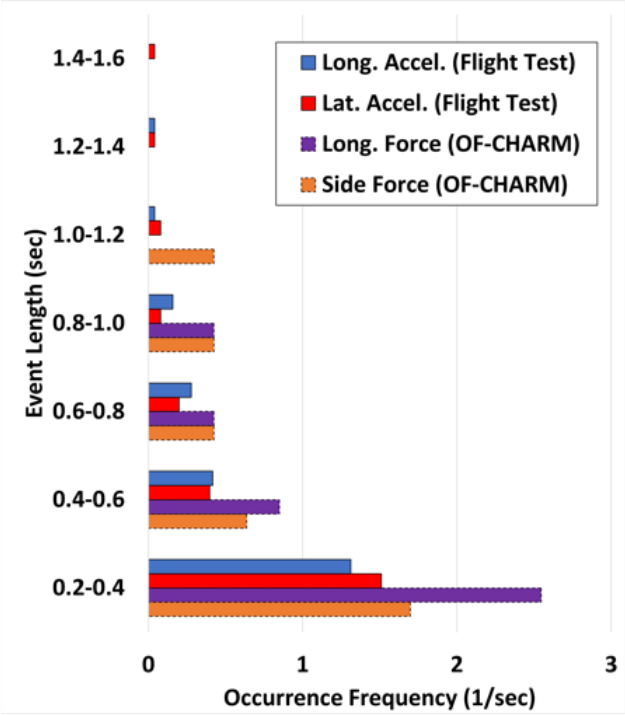

(b) With EFP

Figure 16: Occurrence rate of events of various lengths in time histories of OVERFLOW-CHARM-predicted fuselage longitudinal and side forces and flight test longitudinal and lateral accelerations with and without the EFP.

between CHARM and the airwake database is highly computationally efficient.

7. CONCLUDING REMARKS

This OVERFLOW-CHARM analysis of the physics of the DI provides valuable insight into the capabilities of a state-of-the-art hybrid uRANS/free-wake solver for characterizing DI aerodynamics. OVERFLOW-CHARM can capture the fundamental physical features of the DI at approximately 85% less computational cost than conventional uRANS methods. The effect of DI interactions on unsteady fuselage loads are also correlated with those predicted by flight test data. Analysis of predictions of fuselage force variation indicates that airwake coupling may be vital for accurate characterization of aircraft motion when the helicopter is operating in large regions of separated flow. Coupling OVERFLOW-CHARM to a precomputed airwake database is highly cost efficient, with a less than 0.5% impact on the computational cost compared to uncoupled simulations. The precomputed the airwake can also be re-used for various helicopter positions or for different aircraft models, making it more efficient for routine DI analysis than a unified approach to DI simulation.

As the LOIDR data from the Navy flight test becomes available, quantitative assessments are planned with this hybrid methodology in comparison with other approaches being evaluated for DI applications.

8. ACKNOWLEDGEMENTS

Funding for this work is provided by the Department of Defense (DoD) Science, Mathematics, and Research for Transformation (SMART) scholarship program. Computational resources are allocated through the DoD High Performance Computing Modernization Program (HPCMP) through S/AAA Meghan Goldsborough. Thanks is given to Glen Whitehouse and Dan Wachspress from Continuum Dynamics, Inc. for their invaluable advice and licenses for CHARM, and to Mark Silva, Eric Hayden, and John Tritschler from NAWCAD-PR for developing and distributing the flight test data.

Copyright Statement

9. REFERENCES

[1] Wilkinson, C., VanderVliet, G., and Roscoe, M., "Modeling and Simulation of the Ship-Helicopter Environment," *Proceedings of the Modeling and Simulation Technologies Conference*, American Institute of Aeronautics and Astronautics Inc., Denver, CO, 8 2000, AIAA-2000-4583.

[2] Seth, D., *Contributions to the Understanding of Ship Airwakes Using Advanced Flow Diagnostic Techniques*, Ph.D. thesis, Embry-Riddle Aeronautical University, Daytona Beach, FL, 8 2020, https://commons.erau.edu/edt/533.

[3] Forrest, J. S. and Owen, I., "An Investigation of Ship Airwakes Using Detached-Eddy Simulation," *Computers & Fluids*, Vol. 39, No. 1, 2010, pp. 656–673.

[4] Rosenfeld, N. C., Kimmel, K. R., and Sydney, A. J., "Investigation of Ship Topside Modeling Practices for Wind Tunnel Experiments," 1 2015, AIAA Paper, AIAA-2015-0245, 53rd AIAA Aerospace Sciences Meeting, Kissimmee, Florida.

[5] Quon, E., Smith, M. J., Cross, P., Rosenfield, N., and Whitehouse, G., "Investigation of Ship Airwakes Using a Hybrid Computational Methodology," *Proceedings of the 70th American Helicopter Society Forum*, Montreal, Canada, May 20–22 2014.

[6] Smith, M. J., "Large-Eddy-Simulation-Based Wind Tunnel Assessments," *AVT-284 RWS on Advanced Wind Tunnel Boundary Simulation*, Turino, IT, April 2018.

[7] Crozon, C., Steijl, R., and Barakos, G., "Coupled Flight Dynamics and CFD – Demonstration for Helicopters in Shipborne Environment," *The Aeronautical Journal*, Vol. 122, No. 1247, 11 2018, pp. 42—-82.

[8] Forsythe, J. R., Lynch, E., Polsky, S., and Spalart, P., "Coupled Flight Simulator and CFD Calculations of Ship Airwake using Kestrel," 1 2015, AIAA Paper, AIAA-2015-0556, 53rd AIAA Aerospace Sciences Meeting, Kissimmee, Florida.

[9] Shi, Y., Xu, Y., Zong, K., and Xu, G., "An Investigation of Coupling Ship/Rotor Flowfield Using Steady and Unsteady Rotor Methods," *Engineering Applications of Computational Fluid Mechanics*, Vol. 11, No. 1, 4 2017, pp. 417–434.

[10] Polsky, S. A., Wilkinson, C., Nichols, J., Ayers, D., Mercado-Perez, J., and Davis, T. S., "Development and Application of the SAFEDI Tool for Virtual Dynamic Interface Ship Airwake Analysis," 1 2016, AIAA Paper, AIAA-2016-1771, 54th AIAA Aerospace Sciences Meeting, San Diego, CA.

[11] Quon, E., Smith, M., Whitehouse, G., and Wachspress, D., "Hierarchical Variable Fidelity Methods for Rotorcraft Aerodynamic Design and Analysis," *Proceedings of the American Helicopter Society 67th Annual Forum*, American Helicopter Society Inc., Virginia Beach, Virginia, 1 2011, 67-2011-000309.

[12] Zhao, J. and He, C., "Rotor Blade Structural Loads Analysis Using Coupled CSD/CFD/VVPM," *Proceedings of the American Helicopter Society 69th Annual Forum*, American Helicopter Society Inc., Phoenix, Arizona, 5 2013, 69-2013-040.

[13] Rajmohan, N., *Application of Hybrid Methodology to Rotors in Steady and Maneuvering Flight*, Ph.D. thesis, Georgia Institute of Technology, Atlanta, Georgia, 8 2010, https://smartech.gatech.edu/handle/1853/34756.

[14] Thomas, S., *A GPU-Accelerated, Hybrid FVM-RANS Methodology for Modeling Rotorcraft Brownout*, Ph.D. thesis, University of Maryland, College Park, 1 2013, https://drum.lib.umd.edu/handle/1903/14832.

[15] Jacobson, K. E. and Smith, M. J., "Carefree Hybrid Methodology for Rotor Hover Performance Analysis," *Journal of Aircraft*, Vol. 55, No. 1, 2 2018, pp. 52–65.

[16] Wilbur, I. C., Moushegian, A. M., Smith, M. J., and Whitehouse, G. R., "UH-60A Rotor Analysis with an Accurate Dual-Formulation Hybrid Aeroelastic Methodology," *Journal of Aircraft*, Vol. 57, No. 1, 1 2020, pp. 113–127.

[17] Moushegian, A. M., Smith, M. J., Whitehouse, G. R., and Wachspress, D. A., "Implementation of a Dual-Solver Hybrid Approach for Rotating System Simulations in HPCMP CREATE(TM)-AV HELIOS," 1 2021, AIAA Paper, AIAA-2021-1077, AIAA Scitech 2021 Forum, Virtual Event.

[18] Moushegian, A., Smith, M. J., Whitehouse, G. R., and Wachspress, D. A., "Hover Performance in Ground Effect Prediction Using a Dual Solver Computational Methodology," *Proceedings of the Vertical Flight Society 77th Annual Forum*, Vertical Flight Society Inc., Virtual Event, 5 2021, 77-2021-0200.

[19] Nichols, R. H. and Buning, P. G., *User's Manual for OVERFLOW 2.3*, NASA Langley Research Center, Hampton, VA, Mar. 2021, https://overflow.larc.nasa.gov/users-manual-for-overflow-2-3.

[20] Bliss, D. B., Tenske, M. E., and Quackenbush, T. R., "A New Methodology for Free Wake Analysis Using Curved Vortex Elements," Tech. Rep. NASA-CR-3958, NASA, Dec. 1987.

[21] Bir, G. S., "Structural Dynamics Verification of Rotorcraft Comprehensive Analysis System (RCAS)," Tech. Rep. NREL/TP-500-35328, NREL, Feb. 2005.

[22] Lopes, L. V. and Burley, C. L., "ANOPP2 User's Manual," Tech. Rep. NASA/TM-2016-219342, NASA, Oct. 2016.

[23] Wissink, A. M., Jude, D. P., Jayaraman, B., Roget, B., Laksminarayan, V., Sitaraman, J., Bauer, A. C., Forsythe, J. R., Trigg, R., and Peters, N., "New Capabilities in CREATE-AV Helios Version 11," Jan. 2021, AIAA Paper, AIAA-2021-0235, American Institute of Aeronautics and Astronautics Scitech Forum, Virtual Event.

[24] Keller, J. D., McKillip, Jr., R. M., Wachspress, D. A., Tischler, M. B., and Juhasz, O., "Linearized Inflow and Interference Models from High Fidelity Free Wake Analysis for Modern Rotorcraft Configurations," *Proceedings of the Vertical Flight Society 76th Annual Forum*, Virtual Event, Oct. 2020.

[25] Quackenbush, T. R., Wachspress, D. A., Yu, M. K., , and Solomon, C. L., "Modeling of Proprotor / Wing / Flap Interaction for Advanced Vertical Lift Aircraft," *Proceedings of the Vertical Flight Society 76th Annual Forum*, Virtual Event, Oct. 2020.

[26] Keller, J. D., Sharma, A., Wachspress, D. A., Horn, J. F., and Theron, J. P., "Toward an Urban Air Mobility Ride Quality and Safety Assessment Analytical Tool," *Proceedings of the Vertical Flight Society's 9th Biennial Autonomous VTOL Technical Meeting*, Virtual Event, Jan. 2021.

[27] Quackenbush, T. R., Wachspress, D. A., Yu, M. K., , and Solomon, C. L., "Proprotor / Wing / Flap Interaction for V/STOL Aircraft with Partial Slipstream Immersion," *Proceedings of the Vertical Flight Society's 9th Biennial Autonomous VTOL Technical Meeting*, Virtual Event, Jan. 2021.

[28] Moushegian, A. M., *Dual-Solver Computational Modeling of Ship-Helicopter Dynamic Interface Aeromechanics*, Ph.D. thesis, Georgia Institute of Technology, Atlanta, Georgia, 5 2022, https://smartech.gatech.edu/handle/1853/66581.

[29] Silva, M. J., Hayden, E. W., Myers, L. M., Tritschler, J. K., and Holder, J. M., "Full-Scale Investigation of Rotor/Obstacle Interactions using an Elevated Fixed Platform," *Proceedings of the Vertical Flight Society 78th Annual Forum*, Vertical Flight Society, Ft. Worth, Texas, 5 2022.

[30] McDaniel, D. R. and Tuckey, T., "HPCMP CREATE(TM)-AV Kestrel New and Emerging Capabilities," 1 2020, AIAA Paper, AIAA-2020-1525, AIAA SciTech Forum, Orlando, Florida.

[31] Helden Aerospace Corporation, *HeldenMesh User Manual, Version 3.08*, Helden Aerospace Corporation, 1 2020.

[32] "Helden Aerospace Website," https://heldenaero.com/heldenmesh/, Accessed: 2022-3-24.

[33] Ratnayake, N. A., Krist, S. E., Ghaffardi, F., and Ahmed, V., "Unstructured Grid Development for the Space Launch System Liftoff and Transition Lineloads Computational Analysis," 1 2020, AIAA Paper, AIAA-2020-0672, AIAA SciTech Forum, Orlando, Florida.

[34] Wilbur, I. C., Moushegian, A., Smith, M. J., and Whitehouse, G. R., "Complex Vehicle Design and Analysis with Hybrid Methodologies," *Proceedings of the AHS Aeromechanics Design for Transformative Vertical Flight Meeting*, American Helicopter Society Inc., San Francisco, California, 1 2018, sm_aeromech_2018_44.

[35] Quackenbush, T. R., Boschitsch, A. H., and Wachspress, D. A., "Fast Analysis Methods for Surface-Bounded Flows with Applications to Rotor Wake Modeling," *Proceedings of the American Helicopter Society 52nd Annual Forum*, American Helicopter Society Inc., Washington, D. C., 6 1996.

[36] Lee, R. G. and Zan, S. J., "Wind Tunnel Testing of a Helicopter Fuselage and Rotor in a Ship Airwake," *Journal of the American Helicopter Society*, Vol. 50, No. 4, 10 2005, pp. 326–337.